Framework short-range order observed in a spinel-type Li superionic conductor

Yu Chen[1,2,†], Caleb Ramette[3,†], Matthew Krogstad[4], Maxim Avdeev[5], Erick Lawrence[3,6], Satya Kushwaha[7,8], Chao-Chun Wei[3], Rajavallipuram Sankaran Subramanian[9], Birender Singh[10], Bin Liu[3], Xiaoping Wang[11], Christina M. Hoffman[11], Jue Liu[11], Paul Cardon[3], Kenneth S. Burch[10], Gopalakrishnan Sai Gautam[9], Huiwen Ji[3,*]

[†]Equal contribution

[1] Department of Materials Science and Engineering, University of California, Berkeley, Berkeley, CA, 94720, USA
[2] The Molecular Foundry, Lawrence Berkeley National Laboratory, Berkeley, CA, 94720, USA
[3] Department of Materials Science and Engineering, University of Utah, Salt Lake City, UT, 84112, USA
[4] Materials Science Division, Argonne National Laboratory, Lemont, IL, 60439, USA
[5] Australian Nuclear Science and Technology Organisation, Locked Bag 2001, Kirrawee DC NSW 2232, Australia
[6] Materials Department and Materials Research Laboratory, University of California Santa Barbara, Santa Barbara, CA, 93106, USA
[7] Department of Chemistry, The Johns Hopkins University, Baltimore, MD, 21218, USA
[8] Platform for the Accelerated Realization, Analysis and Discovery of Interface Materials (PARADIM), Department of Chemistry, The Johns Hopkins University, Baltimore, MD, 21218, USA
[9] Department of Materials Engineering, Indian Institute of Science, Bangalore, 560012, India
[10] Department of Physics, Boston College, Chestnut Hill, MA, 02467, USA
[11] Neutron Scattering Division, Oak Ridge National Laboratory, Oak Ridge, TN, 37831, USA

** Corresponding author:*
Prof. Huiwen Ji (Email: huiwen.Ji@utah.edu)

This document contains:

Supplementary Notes 1-5

Supplementary Tables S1-7

Supplementary Figures S1-26

Supplementary References 1-3

Supplementary Note 1. For the refinement of neutron single-crystal diffraction data, the In/Sn occupancy was established by scanning electron microscopy-energy dispersive X-ray spectroscopy (SEM-EDX), elemental analysis and single-crystal XRD. ICP-OES and EDX on the as-grown crystals confirmed that the final In/Sn atomic ratio is ~9:1.1, as shown in Table S1 and Figure S3. Although the elemental analysis reflects the average composition that also includes a minor Li_3InO_3 phase (Figure S2), given its minor portion (3.9 wt%), we do not expect it to significantly alter the In/Sn ratio in the target phase. Refinement of single-crystal XRD data indicates that the total In/Sn occupancy is ~86% in the 16*d* site while nearly none (~3%) in the 16*c* site, as shown in Tables S6-S7. Accordingly, for neutron data analysis, we fixed the In/Sn ratio at 9:1.1 while refining their total occupancy in 16*d* and assigned 0% In/Sn in 16*c*. The rest of 16*d* and the entirety of 16*c* were refined with Li occupancy while both sites were capped at 100% occupancy. An additional constraint was applied to enforce charge balance between all cations and anions, i.e., the total positive valence of Li^+, In^{3+}, and Sn^{4+} should be the same as the total negative valence of O^{2-}.

Supplementary Note 2. MC simulations with varied chemical and size-effect correlations.

Based on Figure S7, the chemical correlations between 16*d* sites that are $< \pm¼, \pm¼, 0>$ and $<\pm½, \pm½, 0>$ apart must both be negative. In other words, their energy terms J_1 and J_2 must both be positive. Their relative dominance modifies intensity distribution, that is, a stronger correlation at $< \pm¼, \pm¼, 0>$ leads to a sharper alternating square pattern that better matches the observation. The negative chemical correlations were also corroborated by 3D-ΔPDF when the corresponding square-shaped diffuse scattering is better isolated (Figure S9b).

Size-wise, an expanded nearest In-In distance and a shrunk In-Li distance produce streaks and block-shaped blocks. The block-shaped feature modulates the intensity distribution in the streaks and is marked out in Figure S8c for visualization. These features become sharper with a stronger size effect from Figures S8c to 8f. Expanding the In-Li distance instead of shrinking removes the block-shaped features and instead creates diffuse blobs around Braggs (Figure S8g). If 16*d* contains no Li substitution (Figure S8h), an expanded In-In distance in a pure size-effect model leads to very strong diffuse streaks.

To reproduce the observed diffuse scattering, we thus selected negative chemical correlations with slight dominance in J_1 over J_2, together with an expanded In-In distance and a shrunk In-Li distance at a reasonable deviation to not overwhelm the chemical SRO features.

Supplementary Note 3. The observed and the modeled 3D-ΔPDF over short distances are shown in Figure S9a-c. Increasing the punch size from a to b better removes near-Bragg diffuse scattering to isolate SROs in the immediate vicinity of atoms. Comparison of observed and modeled 3D-ΔPDF over a longer range is shown in Figure S9d-g. Longitudinal and transverse displacements are seen in d for which a small punch size is used to reserve the near-Bragg diffuse scattering. Switching to a larger punch in e, the collective displacements decay noticeably quicker over

distance, e.g., the split positive intensity at <2, 0, 0> becomes absent. The MC model containing combined chemical SROs and size effect reproduces the transverse displacements for the face-diagonal vectors to some extent (Figure S9f). A pure size-effect MC model without Li substitution in 16*d* produces undisrupted and strong transverse displacements. But the longitudinal displacements in <100> directions are not seen in either model.

Supplementary Note 4. Analysis of the distribution of electrostatic Li site energies

We analyzed the distribution of Li site energies in the spinel-like structure to understand how chemical SRO and structural distortion affect the Li conductivity. A discrete site energy distribution, characterized by narrower groups of Li sites possessing significantly different site energies than others, typically indicates slower Li movement across a structure since Li ions have to at least overcome the difference in energies between the different site groups. Conversely, a continuous distribution of Li site energies suggests a flatter energy landscape for Li motion across the structure, facilitating Li-ion transport. Thus, site energy distributions can be used to estimate the ease of ionic motion in solids, which has been demonstrated in previous study of high-entropy solid electrolytes[1]. Note that analyzing the site energy distribution is a proxy, and not a replacement, to estimating diffusivities via ab initio molecular dynamics simulations or the nudged elastic band method.

We investigated two variants of the Li-In-O system (all Sn is treated as In in the calculation) by: one with chemical SRO only (which introduces Li for In substitution in 16*d*), and another incorporating both chemical SRO and structural distortion due to the local size effect (that is, expanded nearest In-In distances and shrunk nearest In-Li distances). The workflow we followed is illustrated in Figure S21a. Initially, by MC simulation, we created an $8 \times 8 \times 8$ supercell for each variant. For DFT computational feasibility, we subsequently divided the $8 \times 8 \times 8$ supercell into 64 smaller $2 \times 2 \times 2$ domains and applied an Ewald energy[2]-based screening criterion to reduce the number of domains by selecting the 'top' 10 domains (i.e., lowest 10 electrostatic energy supercells) as representatives from each variant for further calculations.

We employed the 'proton-probe' method to determine the site energy of a specific Li site within a $2 \times 2 \times 2$ domain. Specifically, the method involves replacing the Li site of interest with a proton and allowing the proton to relax within a fixed lattice and ionic environment via DFT calculations. The resultant DFT-calculated energy represents the electrostatic site energy of the Li site that was replaced by the proton. The process of replacing Li with proton can be repeated, one-at-a-time, to obtain site energies of all available Li sites in a given structure. To eliminate the influence of 'boundary effects' resulting from our division of the $8 \times 8 \times 8$ supercell into smaller $2 \times 2 \times 2$ domains, we calculated site energies only from the central $1 \times 1 \times 1$ portion of each $2 \times 2 \times 2$ domain. Note that while protons replaced Li sites only from the central $1 \times 1 \times 1$ portion, the DFT calculations included the whole $2 \times 2 \times 2$ domain, thus including longer range interactions that influence the electrostatic site energies as well.

Figures S21b, c display the Li site energy distributions for the two variants. The horizontal axis represents the deviation of site energies from the mean, normalized by the total number of

atoms in the domain. The vertical axis represents the number of Li sites within a given energy range, with each bar spanning over a width of 0.08 eV/atom. Notably, Figure S21b reveals a fairly discrete distribution of Li site energies for the variant with chemical SRO only. The discrete distribution is characterized by the noticeable gaps (or lack of Li sites) in the −0.3 to −0.2 eV/atom and 0 to 0.2 eV/atom ranges, alongside a prominent peak in the 0.2 eV/atom window. Conversely, Figure S21c exhibits a flatter, more continuous distribution with both chemical SRO and structural distortion. For instance, there are no gaps in any range from −0.4 to +0.2 eV/atom, indicating a flat energy landscape that is conducive for fast Li transport.

Supplementary Note 5. Analysis of powder synthesis results of framework substitution

To investigate framework substitution, additional attempts were made to synthesize powders with the initial compositions of $Li_{17}In_9SnO_{24}$ (LISO) as a baseline, $Li_{17}In_9TiO_{24}$ (LITO), $Li_{17}In_9ZrO_{24}$ (LIZO), $Li_{18}In_9ScO_{24}$ (LIScO), $Li_{17}In_{8.55}Sc_{0.45}SnO_{24}$ (LISScO-5%), and $Li_{19}In_8NbO_{24}$ (LINO) using a solid-state method. The same method was used in a previous report[3] to synthesize powder LISO with a final stoichiometry $Li_{15}In_9SnO_{23}$ from the initial composition $Li_{17}In_9SnO_{24}$. The synthesis results were examined by powder XRD, shown in Figure S22. Preliminary Rietveld refinement was performed to identify and estimate phase fractions, shown in Figures S23-24.

The phase fractions of powder LISO were reported in [3], i.e., 35.5 wt% spinel-like and 64.5 wt% disordered rocksalt (DRX). In Figure S22, the Ti-substituted LITO forms spinel-like and DRX phases just like powder LISO, while the Zr-analogue has no trace of the spinel-like phase. Instead, LIZO exhibits a DRX phase and a Li-rich impurity Li_3InO_3 (Figures S22-23). Notably, the higher-angle shift of common diffraction peaks in LIZO (Figure S22, right) indicates that the lattice of the DRX phase of LIZO is even smaller than that of LITO despite the larger radius of Zr^{4+} (0.72 Å) than Ti^{4+} (0.605 Å). Based on the previous finding about LISO[3], i.e., introducing Li over-stoichiometry into the structure leads to lattice expansion, we suspect that the expanded lattice of LITO is likely an indicator of Li stuffing in the structure. In contrast, in LIZO, the excess Li phase-separates into a Li_3InO_3 impurity, indicating that the over-stoichiometric Li is not successfully incorporated into the main phase. Accordingly, LITO exhibits a high room-temperature ionic conductivity of 0.14 mS/cm (Figure S25) while LIZO has no detectable conductivity.

Meanwhile, despite the similar radius and charge of Sc^{3+} and In^{3+}, the substitution of Sc^{3+} for In^{3+} results in a mixture of $LiInO_2$ and Li_3InO_3 phases but not the spinel-like phase (LIScO and LISScO-5% in Figures S22, S24).

Finally, the Nb-doped LINO primarily forms DRX and Li_3InO_3-like phases, with a small fraction of the spinel-like phase with broad but characteristic peaks (Figures S22, S24).

Table S1. Metal composition of the as-grown LISO measured by inductively coupled plasma optical emission spectroscopy (ICP-OES) elemental analysis (calculated by normalizing In to 9.0).

	Li	In	Sn
Starting	18.7	9.0	1.0
As-grown	16.2(1)	9.00(2)	1.10(1)

Table S2. Refined Structural Parameters of LISO at 300K from Single Crystal Neutron Diffraction. The unit cell was determined as F$d\bar{3}m$ (#227) with a = 8.8373(2) Å. R = 4.75%, wR = 4.36%, GOF = 1.794.

Atom	Type	x	y	z	Occ.	U_{eq} [Å^2]	Site
In1	In	0	0.5	0	0.747(3)	0.0069(2)	16*d*
Sn1	Sn	0	0.5	0	0.0912(3)	0.0069(2)	16*d*
Li0	Li	0	0.5	0	0.161(3)	0.0069(2)	16*d*
O1	O	0.00398(3)	0.74602(3)	0.00398(3)	1	0.00971(6)	32*e*
Li1	Li	0.0225(7)	0.0225(7)	0.0225(7)	0.5	0.064(2)	32*e*
Li2	Li	0.125	0.125	0.125	0.46(2)	0.106(4)	8*a*

Table S3. Anisotropic thermal parameters of LISO at 300K from neutron single-crystal diffraction

Atom	U_{11} (Å^2)	U_{22} (Å^2)	U_{33} (Å^2)	U_{12} (Å^2)	U_{13} (Å^2)	U_{23} (Å^2)
In1	0.0069(2)	0.0069(2)	0.0069(2)	–0.0001(4)	–0.0001(4)	–0.0001(4)
Sn1	0.0069(2)	0.0069(2)	0.0069(2)	–0.0001(4)	–0.0001(4)	–0.0001(4)
Li0	0.0069(2)	0.0069(2)	0.0069(2)	–0.0001(4)	–0.0001(4)	–0.0001(4)
O1	0.0097(2)	0.0097(2)	0.0097(2)	–0.0006(2)	–0.0006(2)	–0.0006(2)
Li1	0.064(4)	0.064(4)	0.064(4)	0.008(4)	0.008(4)	0.008(4)
Li2	0.106(7)	0.106(7)	0.106(7)	0	0	0

Table S4. Refined Structural Parameters of LISO at 100K from Single Crystal Neutron Diffraction.

The unit cell was determined as F$d\bar{3}m$ (#227) with a = 8.8373(2) Å. R = 4.49%, wR = 4.42%, GOF = 1.947.

Atom	Type	x	y	z	Occ.	U_{eq} [Å^2]	Site
In1	In	0	0.5	0	0.752(2)	0.0045(2)	16*d*
Sn1	Sn	0	0.5	0	0.0917(3)	0.0045(2)	16*d*
Li0	Li	0	0.5	0	0.156(3)	0.0045(2)	16*d*
O1	O	0.00379(4)	0.74621(4)	0.00379(4)	1	0.00652(6)	32*e*
Li1	Li	0.021(1)	0.021(1)	0.021(1)	0.5	0.059(3)	32*e*
Li2	Li	0.125	0.125	0.125	0.44(2)	0.076(4)	8*a*

Table S5. Anisotropic thermal parameters of LISO at 100K from neutron single-crystal diffraction

Atom	U_{11} (Å^2)	U_{22} (Å^2)	U_{33} (Å^2)	U_{12} (Å^2)	U_{13} (Å^2)	U_{23} (Å^2)
In1	0.0044(2)	0.0044(2)	0.0044(2)	–0.0002(4)	–0.0002(4)	–0.0002(4)
Sn1	0.0044(2)	0.0044(2)	0.0044(2)	–0.0002(4)	–0.0002(4)	–0.0002(4)
Li0	0.0044(2)	0.0044(2)	0.0044(2)	–0.0002(4)	–0.0002(4)	–0.0002(4)
O1	0.0065(1)	0.0065(1)	0.0065(1)	–0.0003(2)	–0.0003(2)	–0.0003(2)
Li1	0.059(6)	0.059(6)	0.059(6)	0.018(5)	0.018(5)	0.018(5)
Li2	0.076(6)	0.076(6)	0.076(6)	0	0	0

Table S6. Refined Structural Parameters of LISO at 300K from Single Crystal X-ray Diffraction. Note that Li content is not refined and is set such that Li fills the rest of the 16*c*, 16*d* and the entirety of the 8*a* site. In and Sn are not differentiated in the refinement.

The unit cell was determined as F$d\bar{3}m$ (#227) with a = 8.8591(2) Å. R = 1.09%, wR = 2.75%, GOF = 1.390.

Atom	Type	x	y	z	Occ.	U_{eq} [Å^2]	Site
In1	In	0	0.5	0	0.86(2)	0.0082(2)	16*d*
Li0	Li	0	0.5	0	0.14(2)	0.0082(2)	16*d*
O1	O	0.0040(2)	0.7460(2)	0.0040(2)	1	0.0105(8)	32*e*
Li1	Li	0	0	0	0.964(4)	0.030(3)	16*c*
In2	In	0	0	0	0.036(4)	0.030(3)	16*c*
Li2	Li	0.125	0.125	0.125	0.46	0.07(2)	8*a*

Table S7. Anisotropic thermal parameters of LISO at 300K from neutron single-crystal diffraction

Atom	U_{11} (Å^2)	U_{22} (Å^2)	U_{33} (Å^2)	U_{12} (Å^2)	U_{13} (Å^2)	U_{23} (Å^2)
In1	0.0082(2)	0.0082(2)	0.0082(2)	–0.00098(6)	–0.00098(6)	–0.00098(6)
Li0	0.0082(2)	0.0082(2)	0.0082(2)	–0.00098(6)	–0.00098(6)	-0.00098(6)
O1	0.0105(8)	0.0105(8)	0.0105(8)	0.0005(5)	–0.0005(5)	0.0005(5)
Li1	0.030(3)	0.030(3)	0.030(3)	–0.0001(14)	–0.0001(14)	–0.0001(14)
In2	0.030(3)	0.030(3)	0.030(3)	–0.0001(14)	–0.0001(14)	–0.0001(14)
Li2	0.07(2)	0.07(2)	0.07(2)	0	0	0

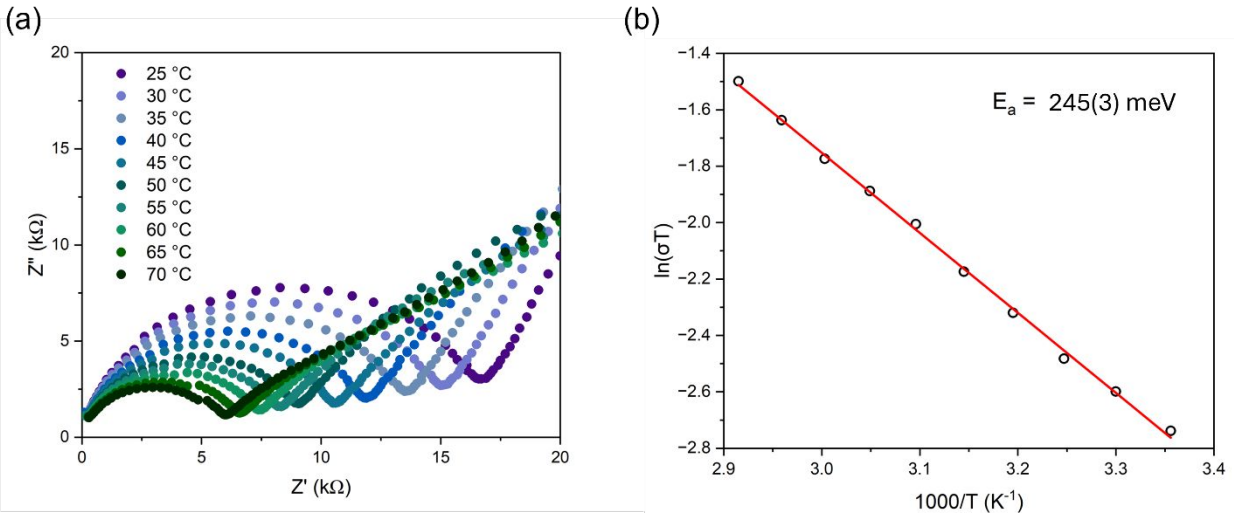

Figure S1. (a) Nyquist plots measured on a piece of polished floating-zone grown sample containing multiple domains (0.0221 cm^2 in area and 0.080 cm in thickness) at various temperatures and (b) the Arrhenius-fit and activation energy.

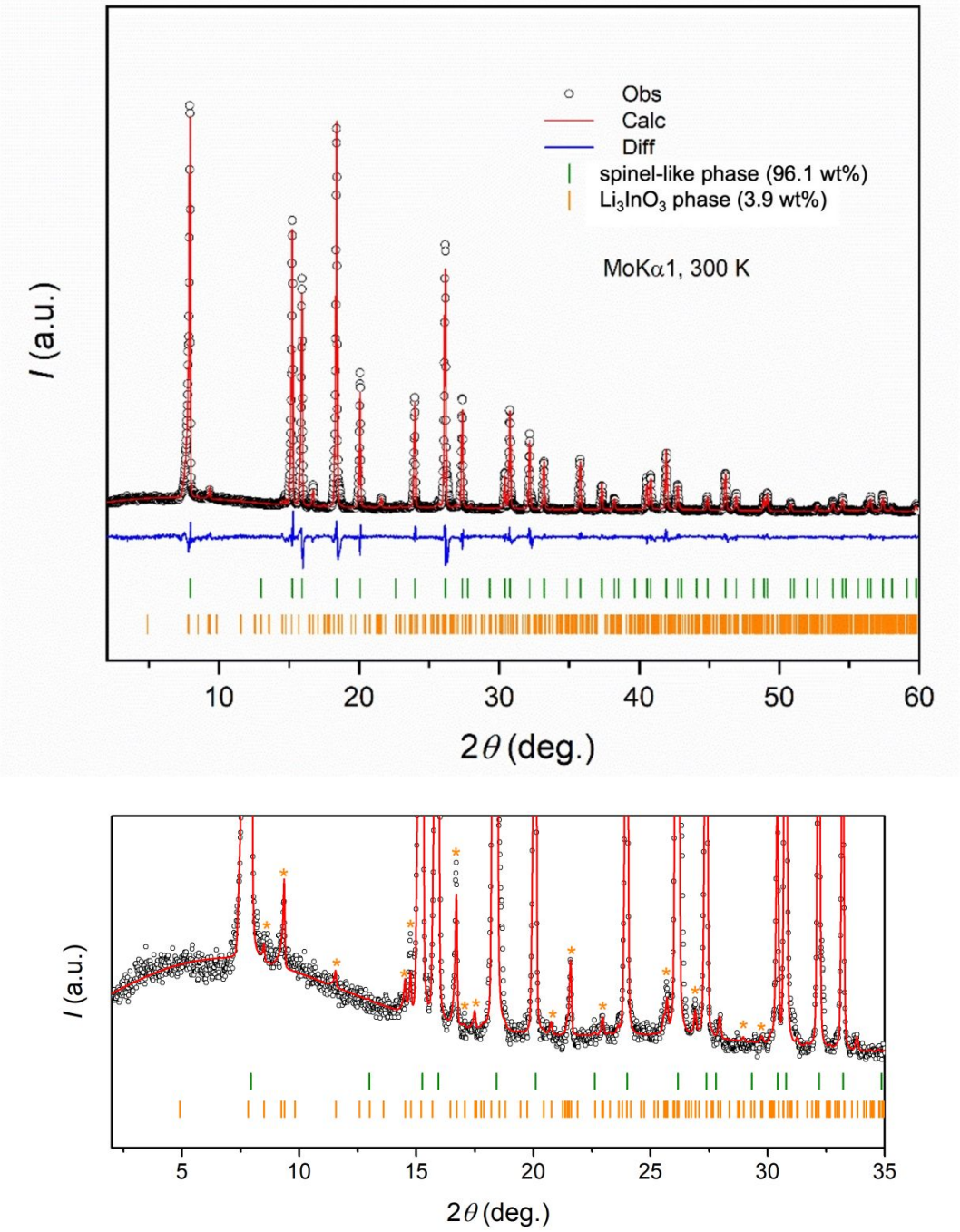

Figure S2. (upper panel) Refined powder X-ray diffraction pattern of ground LISO crystals grown by a floating-zone method. Observed data, fit, difference, and Bragg positions (of the main spinel-like phase and an impurity Li_3InO_3 phase) are represented by black open circles, solid red line, solid blue line, olive and orange ticks, respectively. (lower panel) Zoom-in view in low-angle range to showcase the fitting of the weak impurity peaks (marked by orange stars). The impurity peaks were well matched by Li_3InO_3 peak positions although there is some intensity discrepancy, likely because of composition deviation, which might lead to error(s) in the determined phase weight ratio.

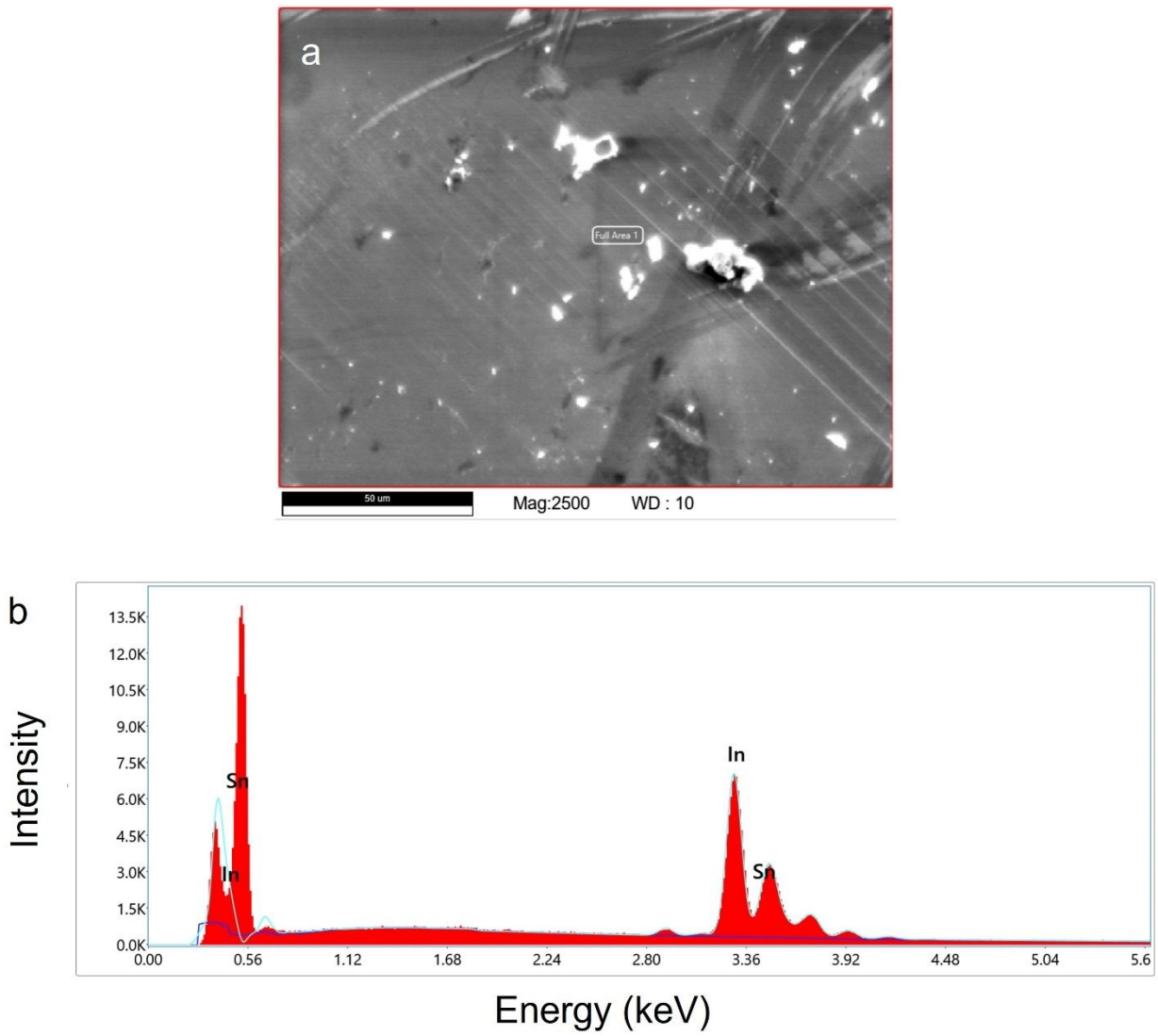

Figure S3. SEM-EDX spectrum measured on a polished LISO crystal surface. (a) SEM image of the LISO crystal, in a secondary electron mode. (b) EDX spectrum fit using the *L* edges of In and Sn. The measured portions of In and Sn are 90.0 at.% (error 4.1%) and 10.0 at.% (error 11.1%), respectively.

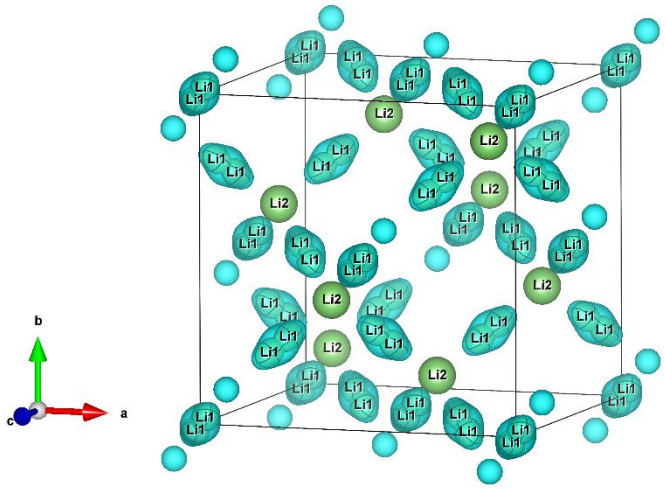

Figure S4. (a) A unit cell refined from neutron data at 300 K. 50% Li ADPs in 8a (Li2) and 32e (Li1) sites are represented by green ellipsoids. Li density isosurfaces are in a translucent cyan color. Several Li2 site isosurfaces are demonstrated outside the unit cell boundary without overlaying on ADP ellipsoids for clarity.

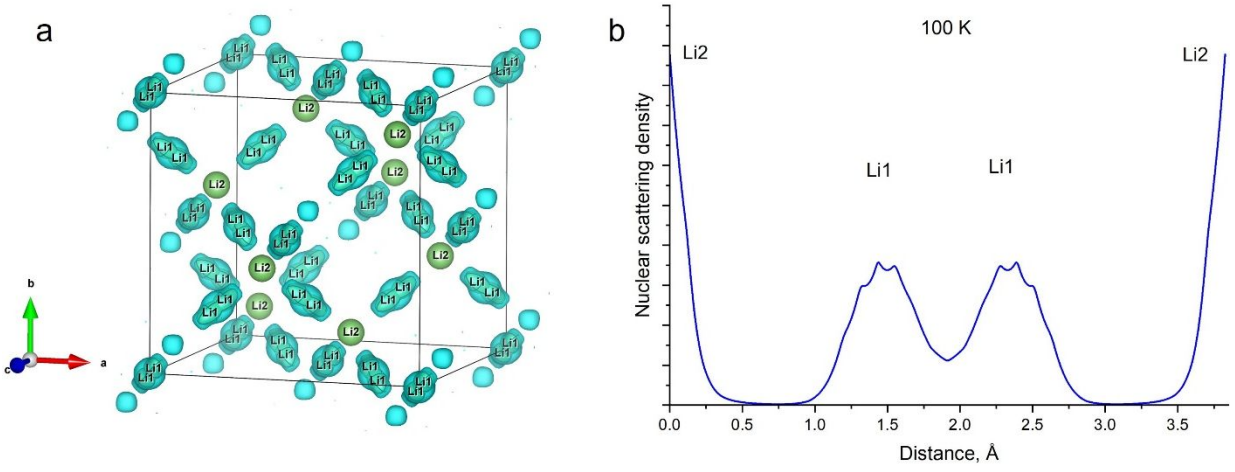

Figure S5. (a) A unit cell refined from neutron data at 100 K. 50% Li ADPs in 8a (Li2) and 32e (Li1) sites are represented by green ellipsoids. Li density isosurfaces are in a translucent cyan color. Several Li2 site isosurfaces are demonstrated outside the unit cell boundary without overlaying on ADP ellipsoids for clarity. (b) Li nuclear density generated from neutron diffraction at 100 K along a Li2-Li1-Li1-Li2 path.

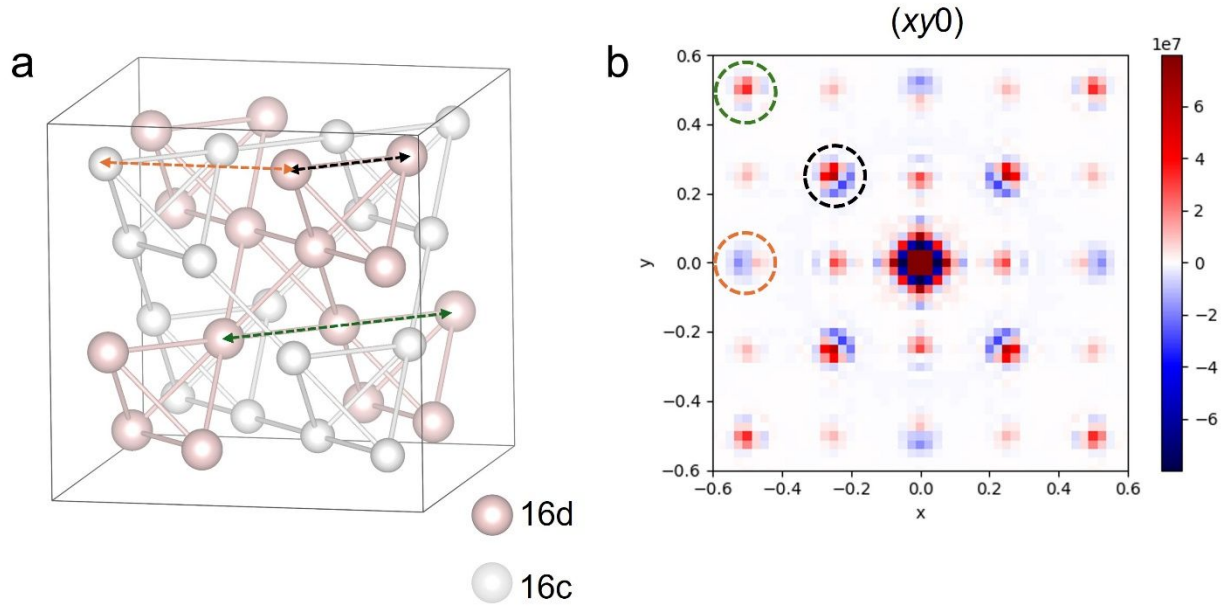

Figure S6. 3D-ΔPDF generated from synchrotron diffuse scattering and the corresponding interatomic pairs in crystal structure. (a) A spinel unit cell showcasing 16*d* and 16*c* sites only. (b) 3D-ΔPDF in the *xy*0 plane. The vectors highlighted by circles in (b) contain major contribution from the atom pairs shown in the crystal structure in (a) with matching colors. These atom pairs all involve In because X-ray is most sensitive to heavy elements.

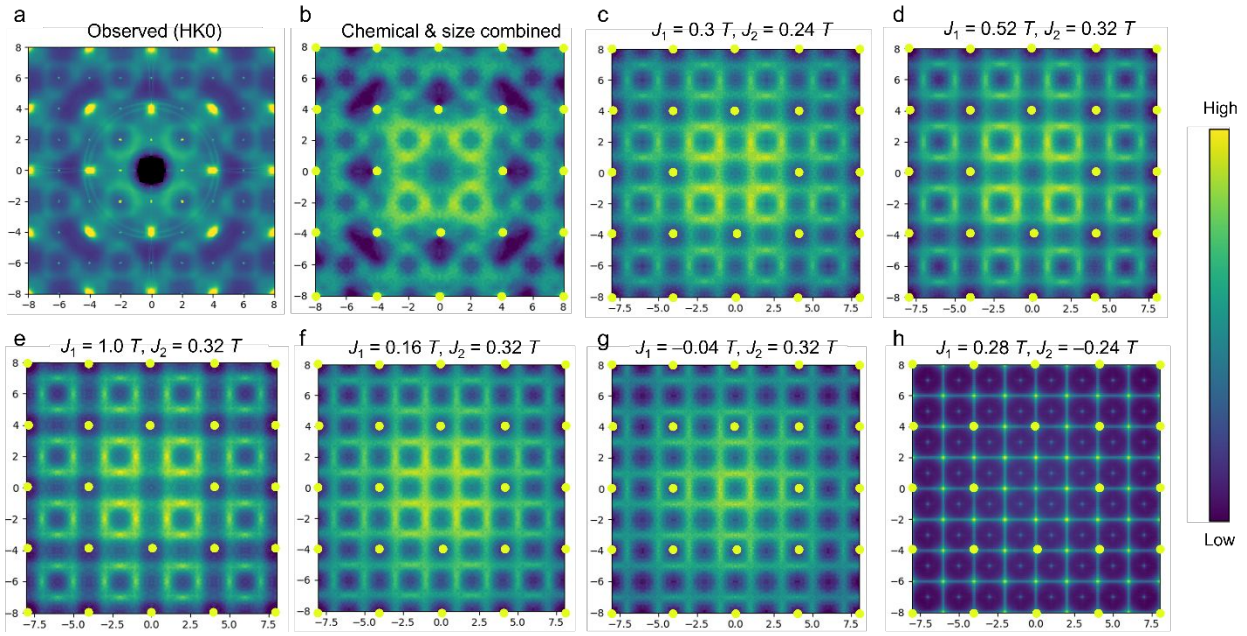

Figure S7. MC modeled diffuse scattering in *HK*0 with various chemical correlation parameters. The observed pattern is shown in **(a)** with the final combined model shown in **(b)** for comparison. **(c)-(h)** were modeled with chemical correlations only in the < ±¼, ±¼, 0> (J_1) and <±½, ±½, 0> (J_2) vectors. The Bragg positions are marked out by yellow dots. No size effect is considered. A positive (negative) sign in ***J*** is equivalent to a negative (positive) chemical correlation and means the In-In pair is disfavored (favored).

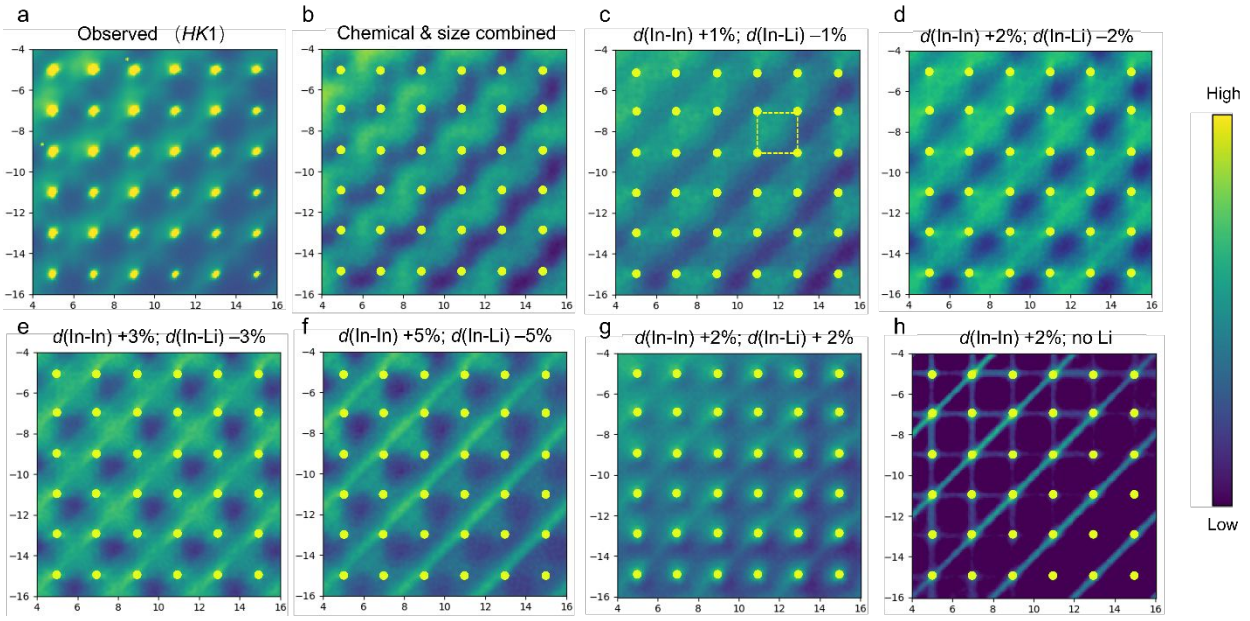

Figure S8. MC modeled diffuse scattering in *HK*1with various size-effect correlation parameters. The observed pattern **(a)** is shown in top left with the final combined model **(b)** shown to its right for comparison. **(c)-(h)** were modeled with the size effect only and various target deviations in the nearest In-In or In-Li distances. In the models, 16*d* contains 15% Li for In substitution that is

randomly distributed. The lower right panel **(h)** shows a model without Li substitution in 16*d*. The Bragg positions are marked out by yellow dots.

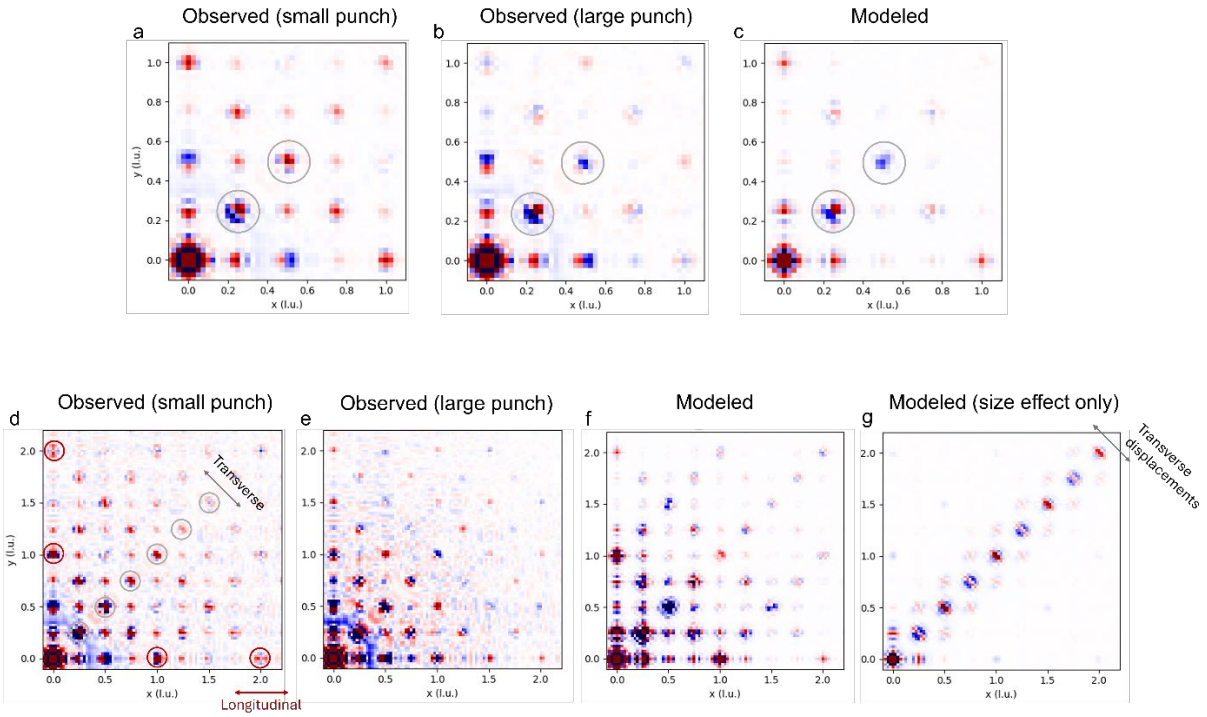

Figure S9. Comparison between observed and modeled 3D-ΔPDF. Observed 3D-ΔPDF at short distances with a small Bragg punch size of 0.2 r.l.u. for **(a)** and a large punch size (of 0.6 r.l.u. for all-even HKL's and 0.45 r.l.u. for all-odd HKL's) for **(b)**, compared with the modeled in **(c)**. Observed 3D-ΔPDF in longer ranges with a small punch size for **(d)** and a large punch size for **(e)**, compared with the combined MC model in **(f)** as well as a size-effect-only MC model in **(g)**.

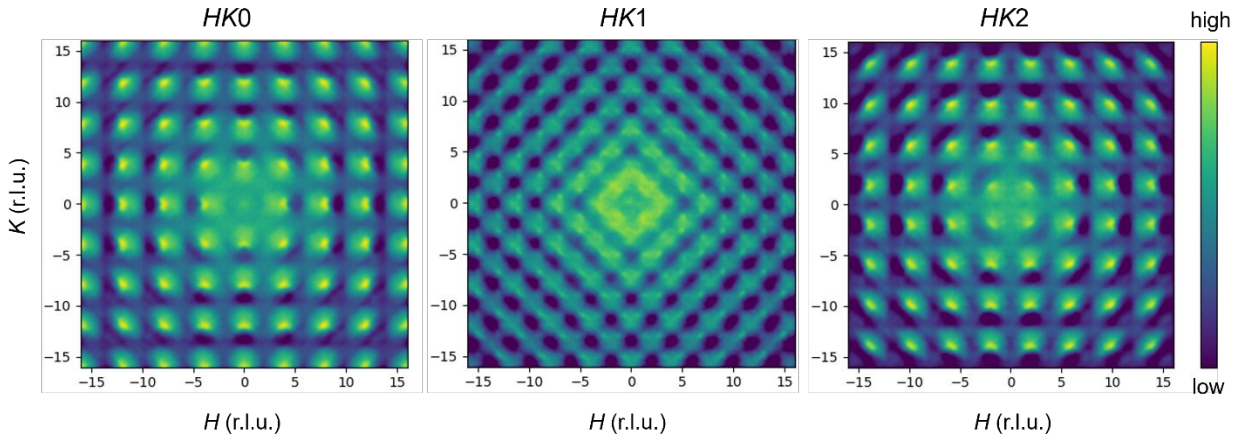

Figure S10. Simulated diffuse scattering patterns with the local size effect only. Intensity on a log scale.

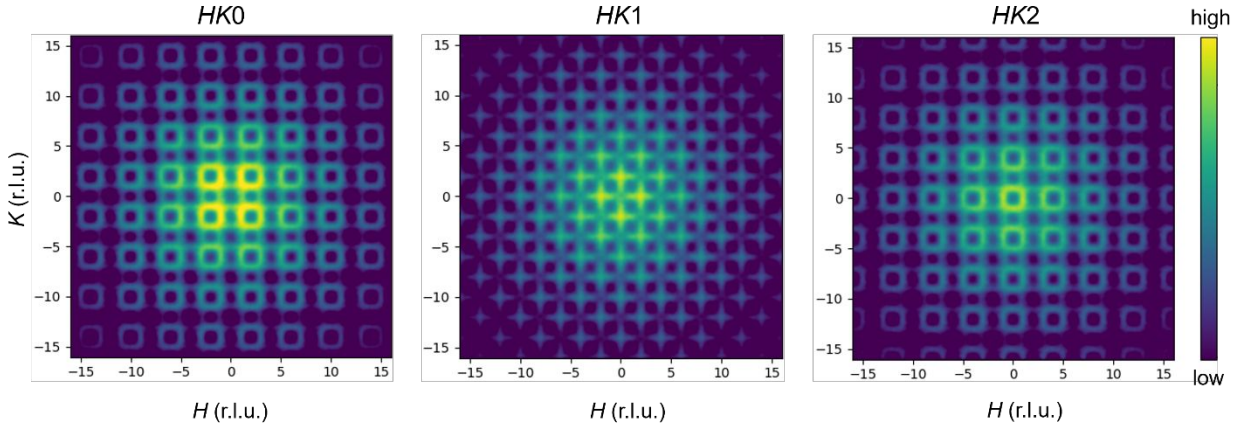

Figure S11. Simulated diffuse scattering patterns with chemical SROs only. Intensity on a log scale.

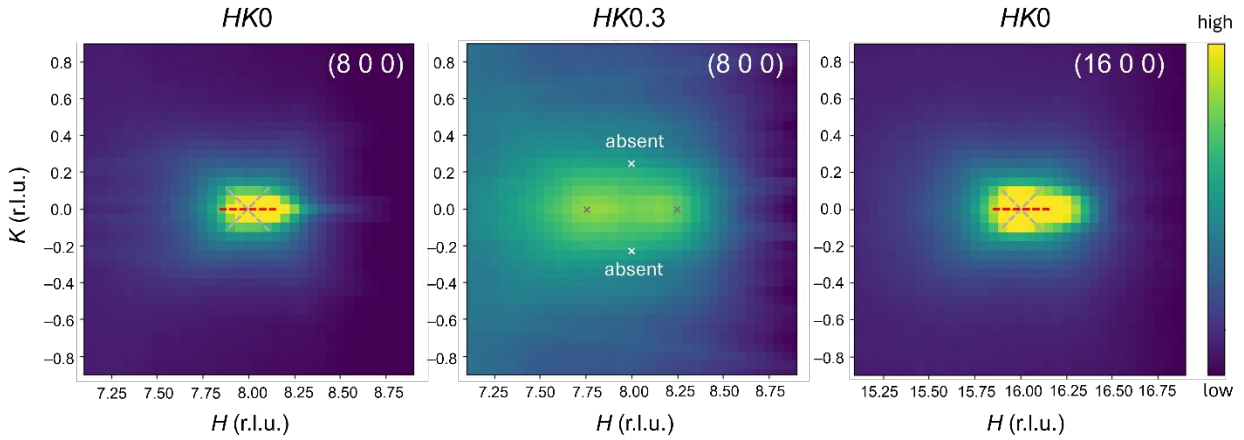

Figure S12. Observed near-Bragg diffuse scattering on a log intensity scale. (left to right) Near (8 0 0) in *HK*0 and *HK*0.3, and near (16 0 0) in *HK*0. Diffuse scattering rods along <100> and <110> directions are highlighted by red and grey lines, respectively. Two grey crosses in the middle panel mark the intersections of [101] and [10$\bar{1}$] rods. The [011] and [01$\bar{1}$] rods are absent. The diffuse scattering is more spread out towards higher $\boldsymbol{Q}$ for (16 0 0) than for (8 0 0) due to the displacive nature of the associated short-range order.

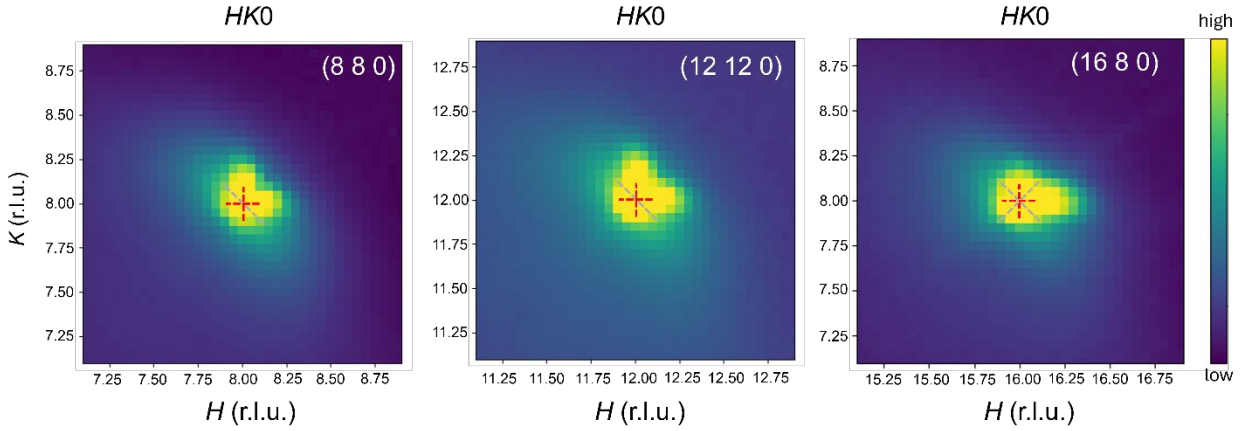

Figure S13. Observed near-Bragg diffuse scattering on a log intensity scale. (left to right) Near (8 8 0), (12 12 0), and (16 8 0) in *HK*0. Diffuse scattering rods along <100> and <110> directions are highlighted by red and grey lines, respectively. The first two Braggs are on a face-diagonal [110] axis, and show two diffuse branches of Type A, i.e., [100] and [010], as well as one [1$\bar{1}$0] branch of Type B. The off-diagonal Bragg (16 8 0) on the right shows a stronger [100] rod than the [010] rod due to a larger *H* component in its Bragg $\boldsymbol{G}$ vector. The diffuse scattering is more spread out towards higher $\boldsymbol{Q}$ due to the displacive nature of the associated short-range order.

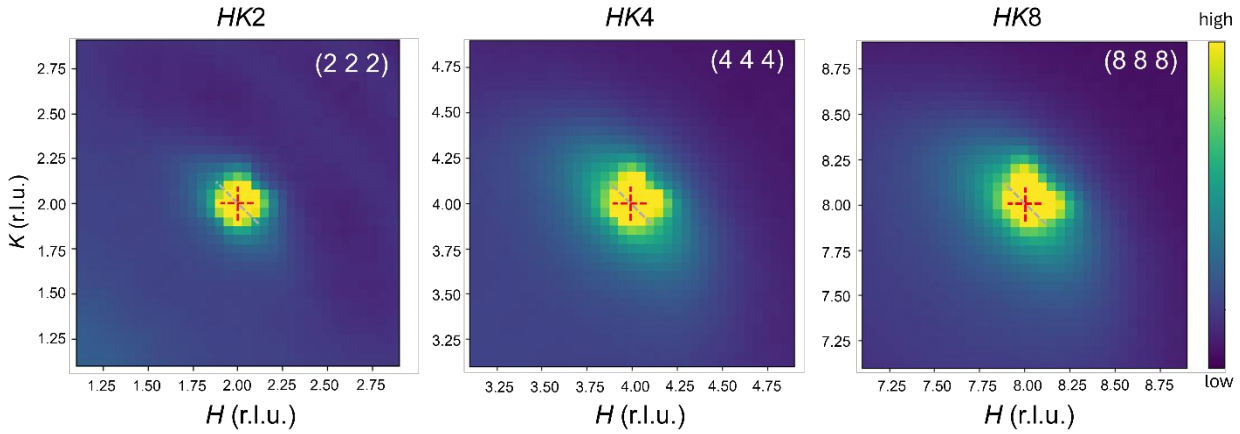

Figure S14. Observed near-Bragg diffuse scattering on a log intensity scale. (left to right) Near (2 2 2), (4 4 4), and (8 8 8). Diffuse scattering rods along <100> and <110> directions are highlighted by red and grey lines, respectively. All three Braggs show two branches of Type A, i.e., [100] and [010], as well as one [$1\bar{1}0$] branch of Type B. Due to the 3-fold rotation around the [111] axis, the [001] rod of Type A and the [$01\bar{1}$] and [$10\bar{1}$] rods of Type B can also be derived, although not immediately seen in the current views. The diffuse scattering is more spread out towards higher ***Q*** due to the displacive nature of the associated short-range order.

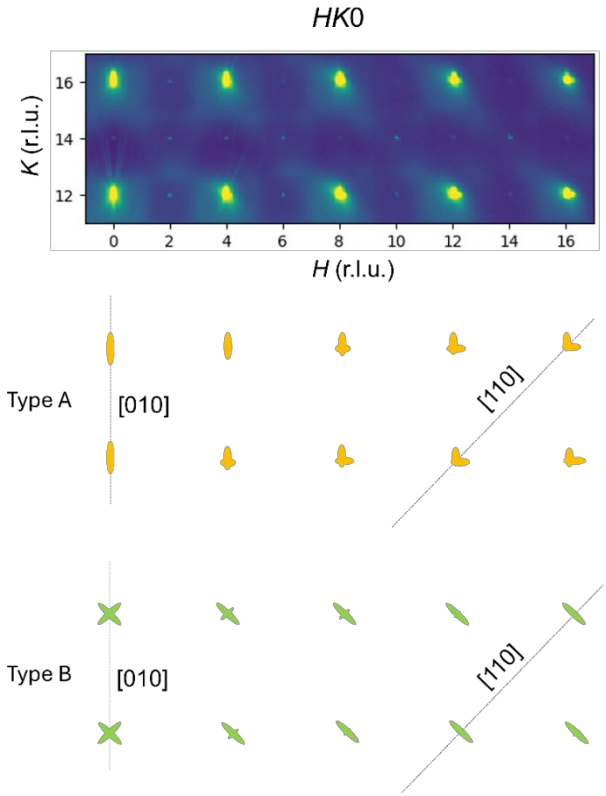

Figure S15. Observed diffuse scattering rods with gradual shift in absence and dominance from Bragg spots on (and away from) the major [010] and [110] axes (top). Schematics of contribution from Type A and Type B are underneath the experimental.

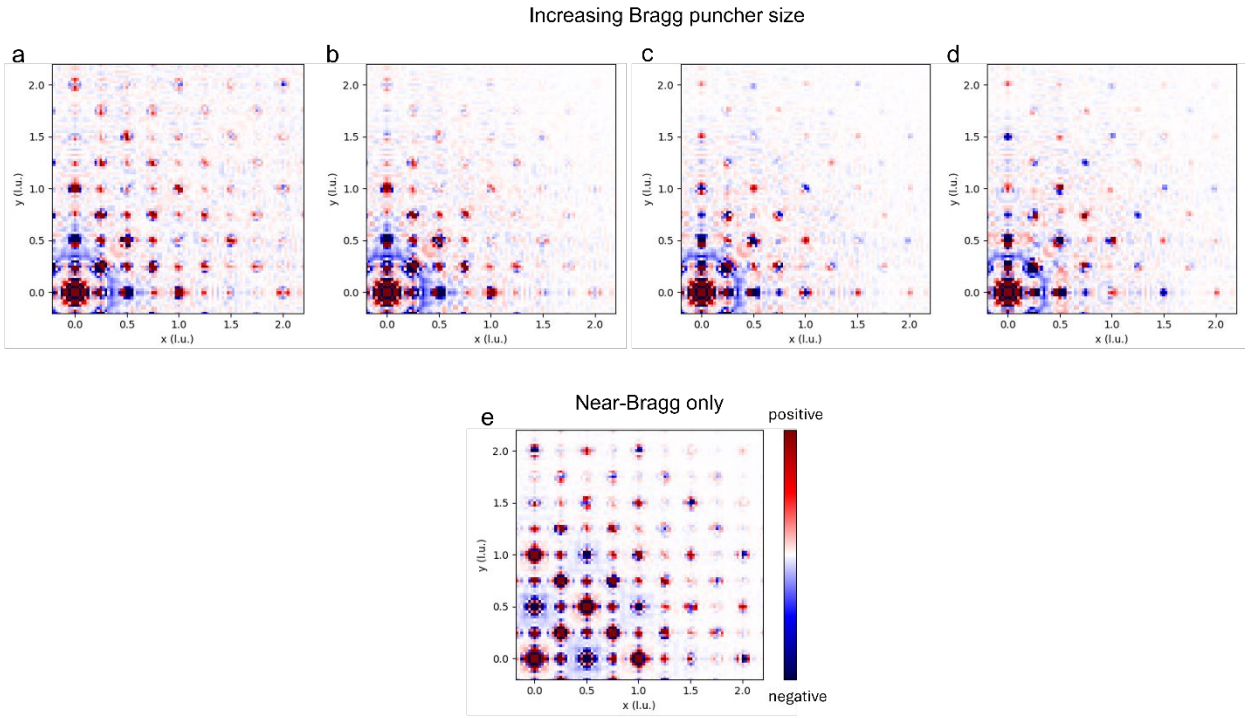

Figure S16. 3D-ΔPDF in *xy*0 generated with an increasing Bragg puncher size: 0.2 r.l.u. radius for **(a)**, 0.3 r.l.u. for **(b)**, 0.6 r.l.u. for all-even *H*, *K*, *L* and 0.45 r.l.u. for all-odd *H*, *K*, *L* for **(c)**, and 1.0 r.l.u. for all-even *H*, *K*, *L* and 0.6 r.l.u. for all-odd *H*, *K*, *L* for **(d)**. The longitudinal displacements in vectors along ***x*** (or ***y***) and the transverse displacements in vectors along face-diagonal gradually disappear from **a** to **d**. **(e)** 3D-ΔPDF from near-Bragg diffuse scattering only with a Bragg puncher size of 0.2 r.l.u. After the Braggs are removed, only signals within 0.5 r.l.u. from Braggs are kept while the diffuse signals more than 0.5 r.l.u. from Braggs are set to 0. Due to the zero background, artificial positive residuals in the first unit cell were created. Nevertheless, beyond the first unit cell, collective displacements are clearly seen.

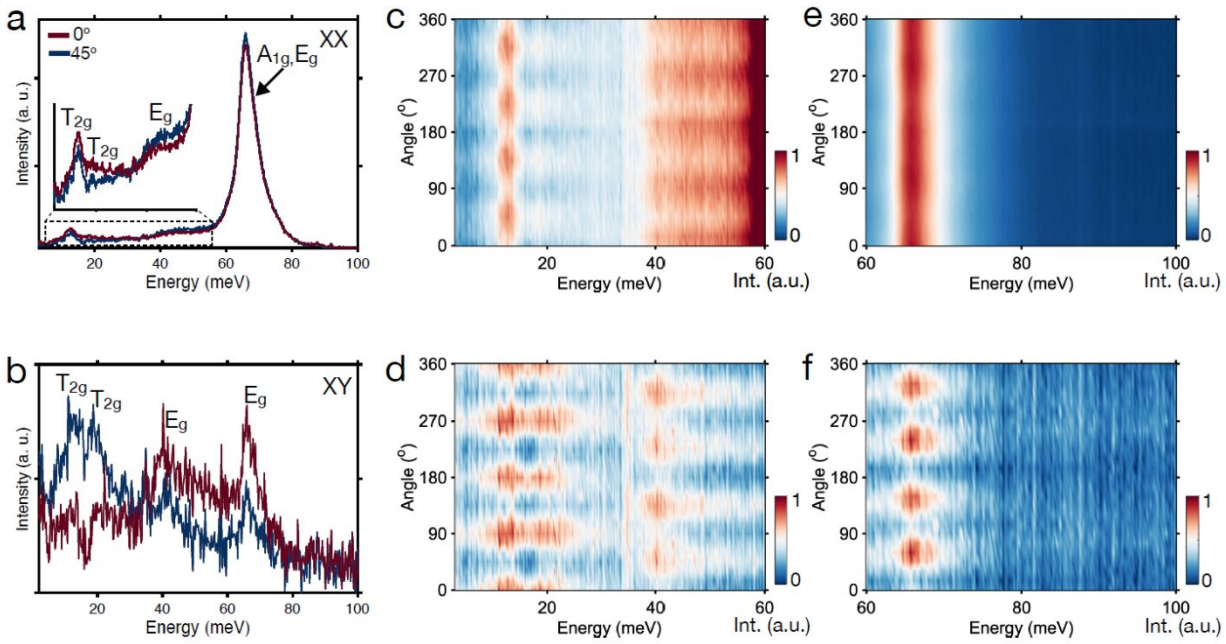

Figure S17. Angle-resolved Raman response of LISO in parallel (XX) and crossed (XY) polarization configurations at 294 K, (a, b) Raman spectra recorded at 0 and 45 deg in (a) XX, and (b) XY configurations (inset in (a) highlights the low-energy spectra features). **(c-f)** Color map illustrating the angular dependence of the Raman spectra in, (c, e) XX, and (d, f) XY polarizations. The symmetry assignments of all observed phonon modes are indicated in (a, b).

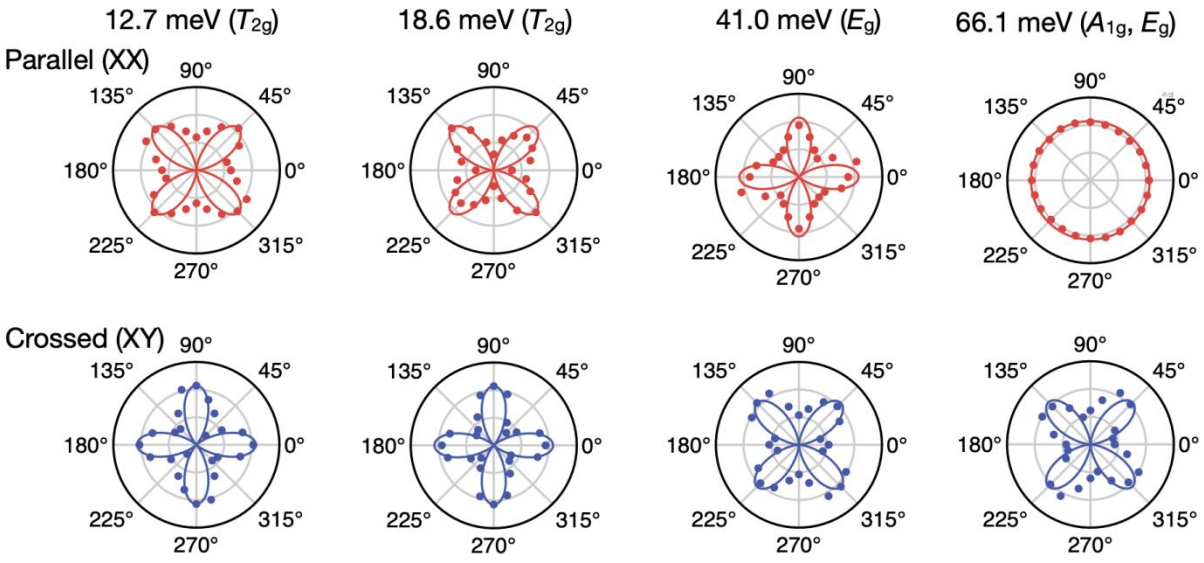

Figure S18. Angular dependence of the phonon mode intensity in parallel (XX) and crossed (XY) polarizations fitted with the Raman tensors of the T_{2g}, E_g, and A_{1g} symmetry of the F$d\bar{3}m$ space group.

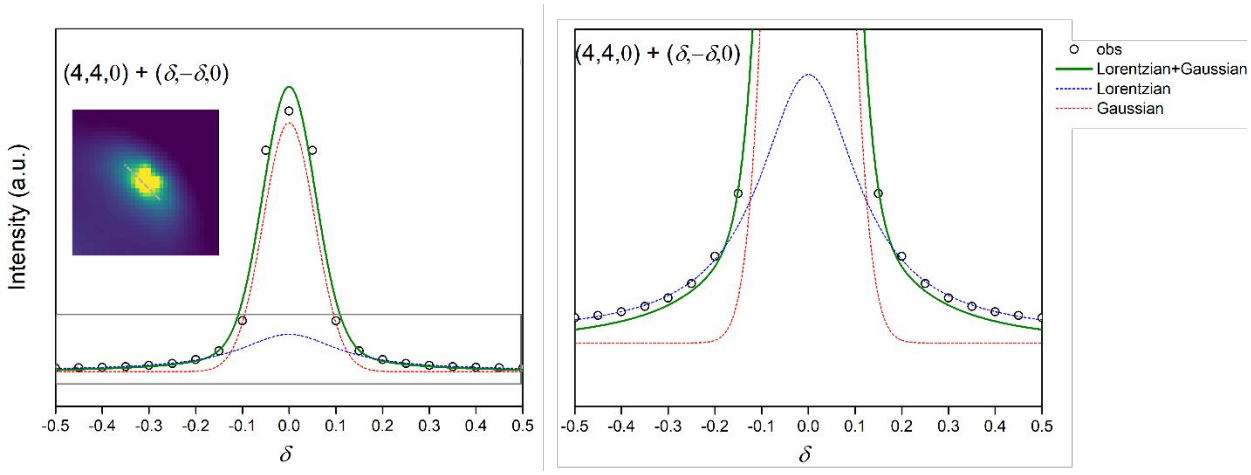

Figure S19. (left) Total scattering intensity along [$1\bar{1}0$] through the (4 4 0) Bragg reflection. The experimentally observed scattering intensity distribution is shown as an inset. Type B diffuse scattering dominates in this direction. A Gaussian and a Lorentzian function are used to fit the Bragg peak (with instrumental broadening) and the near-Bragg diffuse scattering, respectively. A zoom-in view of the boxed region is shown on the right. The estimated correlation length of Type B near-Bragg diffuse scattering based on the Lorentzian fit is ~ 9.6 l.u. or ~ 8.4 nm.

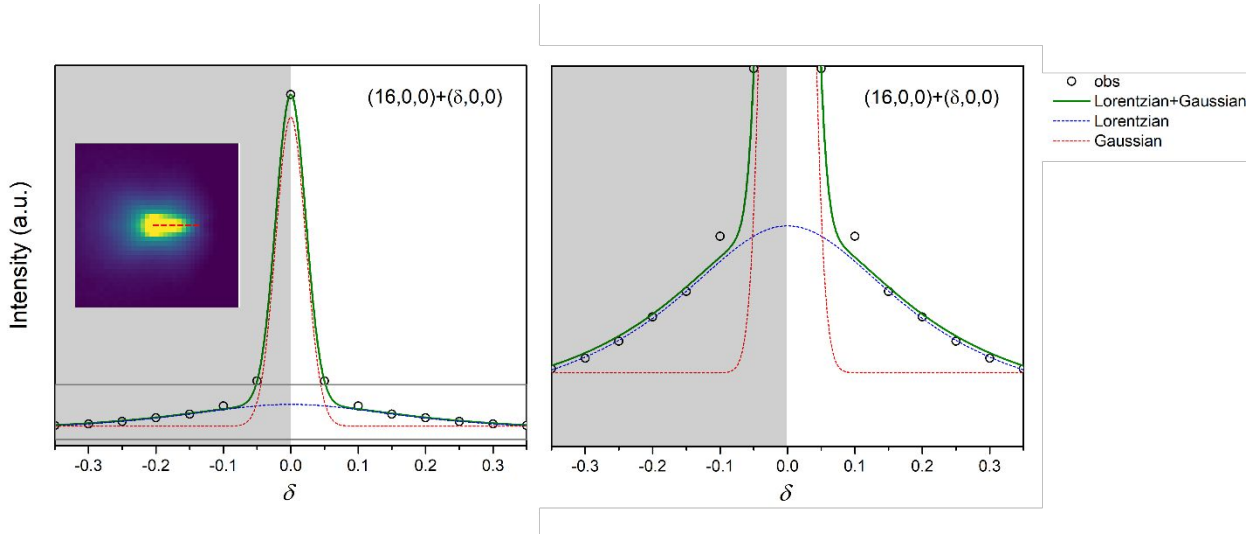

Figure S20. (left) Total scattering intensity along [100] through the (16 0 0) Bragg reflection. The experimentally observed scattering intensity distribution is shown as an inset. Type A diffuse scattering dominates in this direction. A Gaussian and a Lorentzian function are used to fit the Bragg peak (with instrumental broadening) and the near-Bragg diffuse scattering, respectively. A zoom-in view of the boxed region is shown on the right. Due to the asymmetry of Type A diffuse scattering, the intensity values at negative δ's (greyed) are taken by mirroring the positive-δ side. The estimated correlation length of Type A near-Bragg diffuse scattering based on the Lorentzian fit is ~ 4.7 l.u. or ~ 4.1 nm.

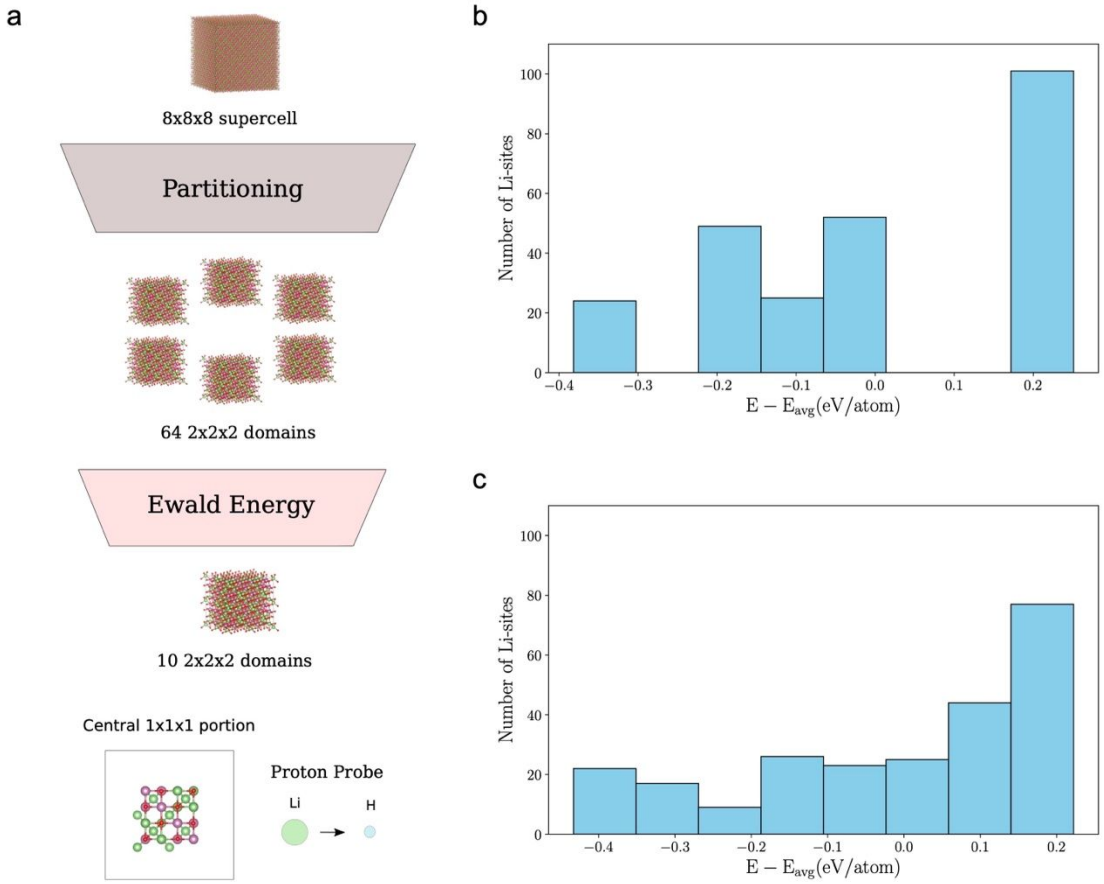

Figure S21. (a) Workflow for calculating electrostatic energy distribution of Li sites in the spinel-like system. Upon generating an 8×8×8 supercell by MC simulation, we partition it into smaller 2×2×2 domains, filter out the 10 lowest energy electrostatic domains, and replace the Li sites in the central 1×1×1 domains with proton one-at-a-time. **(b)** With chemical SRO only, distribution of the deviation of ite energies from the mean. **(c)** Combining both chemical SRO and structural distortion, distribution of the deviation of Li site energies from the mean. Each bin in the histogram corresponds to a 0.08 eV/atom width.

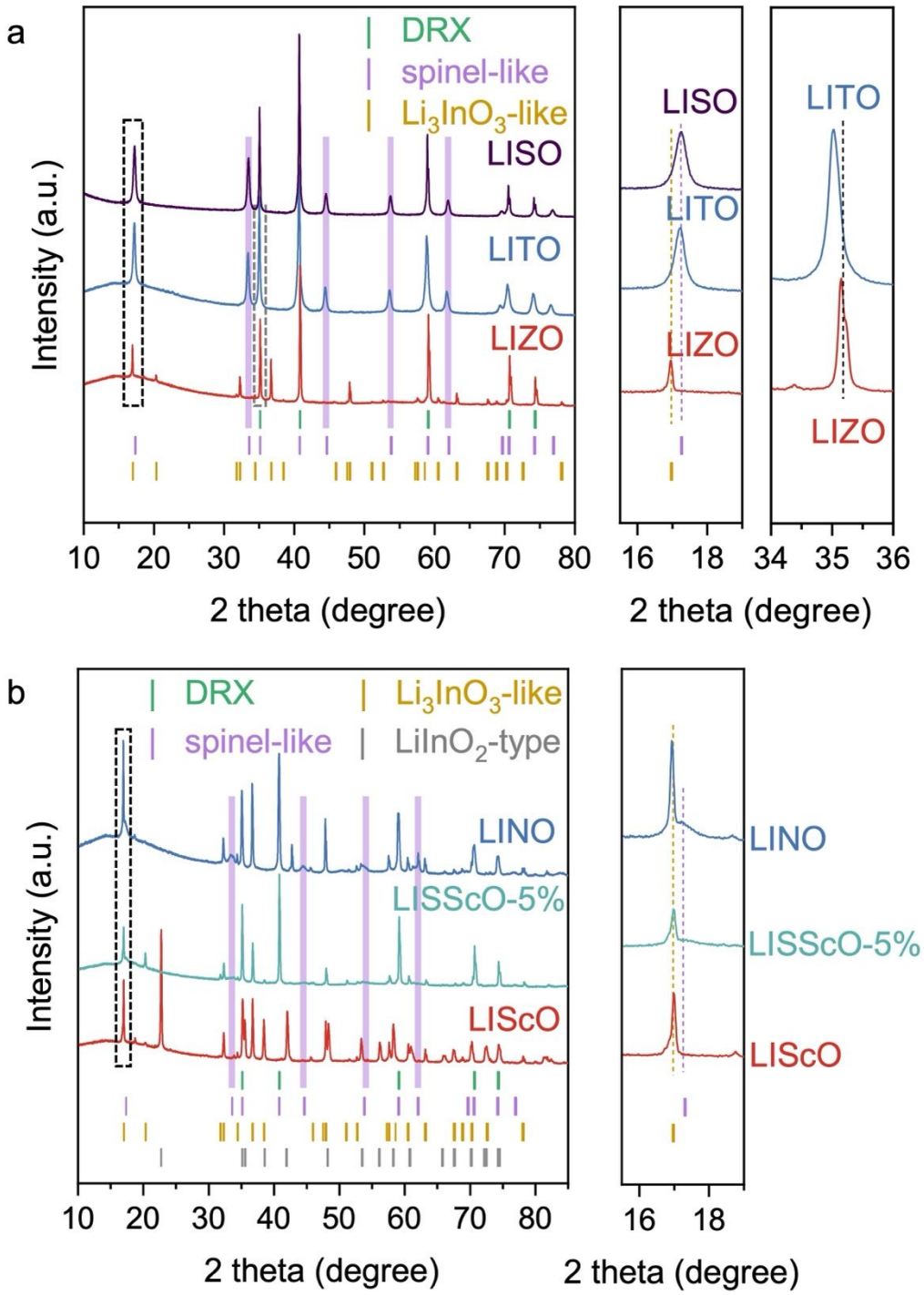

Figure S22. Results of d^0 substitutions in LISO. XRD patterns of (a) powder LISO, LITO, LIZO, and (b) LIScO, LISScO-5%, LINO that were synthesized by a solid-state method. Bragg positions of the phases identified are labelled with vertical ticks: green–disordered rocksalt (DRX), purple–spinel-like, yellow–Li_3InO_3-like, grey–$LiInO_2$-type. The subplots on the right show magnified XRD patterns of the regions highlighted by the dashed boxes. Spinel-characteristic peak positions are highlighted by purple bars.

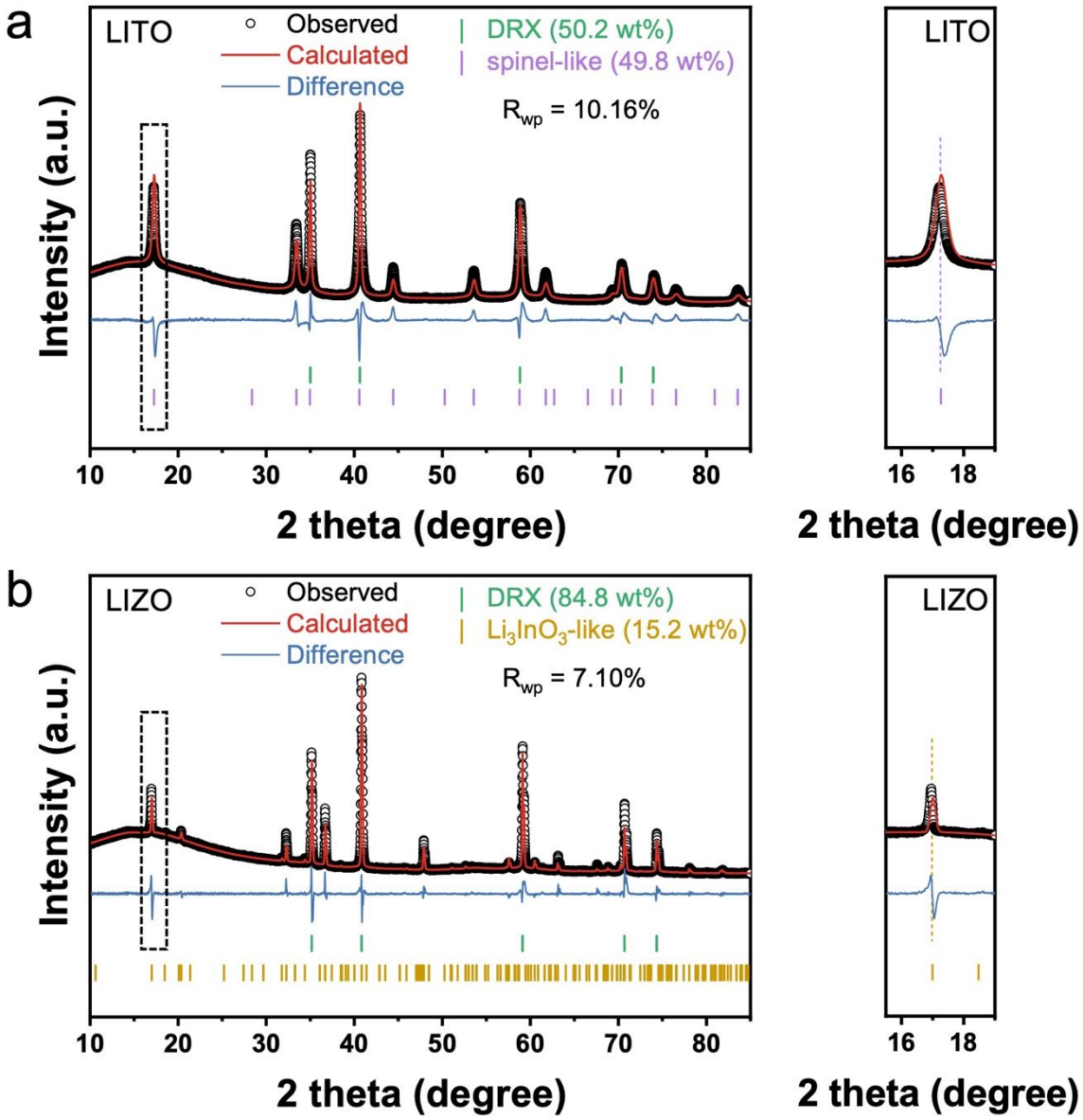

Figure S23. Rietveld refinement of lab XRD data of **(a)** LITO, **(b)** LIZO. The positions of Bragg reflections for the identified phases are indicated by vertical tick marks, and the refined phase weight fractions are shown in the plots. The panels on the right show magnified XRD patterns of the regions highlighted by the dashed boxes. The intensity discrepancy in the refinement likely comes from the fact that the spinel-like and the DRX phases are both refined based on the nominal composition and the compositions of the impurity phases are assumed to be Li_3InO_3, $LiInO_2$, and NbO. The assumption is over-simplified but necessary given the difficulty in determining precise compositions in the multi-phase problem. The intensity discrepancy may compromise the confidence in the refined weight ratio of the various phases.

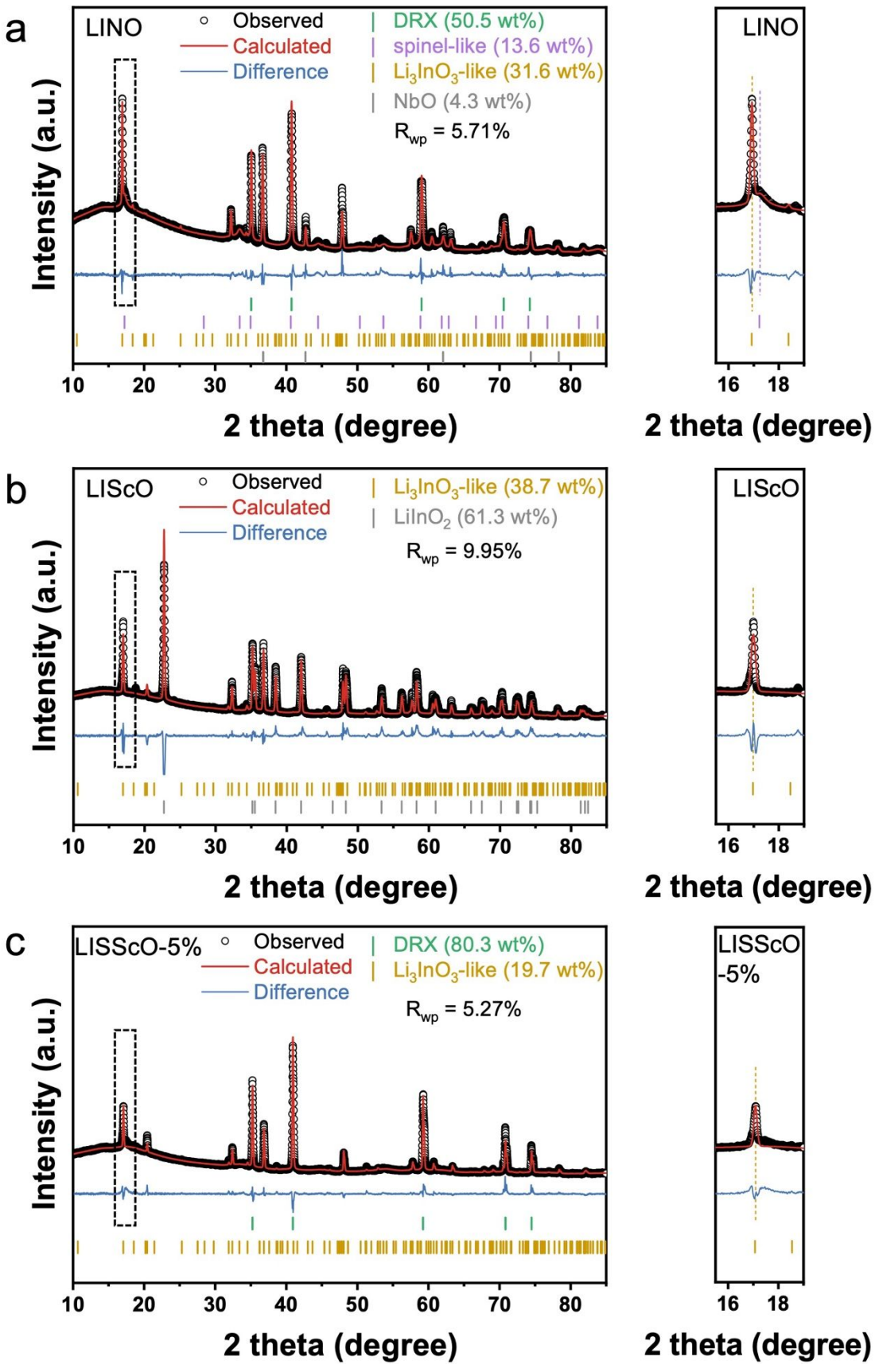
a
LINO
Observed
Calculated
Difference
DRX (50.5 wt%)
spinel-like (13.6 wt%)
Li3InO3-like (31.6 wt%)
NbO (4.3 wt%)
Rwp = 5.71%
Intensity (a.u.)
2 theta (degree)
LINO
b
LIScO
Li3InO3-like (38.7 wt%)
LiInO2 (61.3 wt%)
Rwp = 9.95%
c
LISScO-5%
DRX (80.3 wt%)
Li3InO3-like (19.7 wt%)
Rwp = 5.27%
LISScO -5%

Figure S24. Rietveld refinement of lab XRD data of **(a)** LINO, **(b)** LIScO, **(c)** LISScO-5%. The positions of Bragg reflections for the identified phases are indicated by vertical tick marks, and the refined phase weight fractions are shown in the plots. The panels on the right show magnified XRD patterns of the regions highlighted by the dashed boxes. The intensity discrepancy in the refinement likely comes from the fact that the spinel-like and the DRX phases are both refined based on the nominal composition and the compositions of the impurity phases are assumed to be Li_3InO_3, $LiInO_2$, and NbO. The assumption is over-simplified but necessary given the difficulty in determining precise compositions in the multi-phase problem. The intensity discrepancy may compromise the confidence in the refined weight ratio of the various phases.

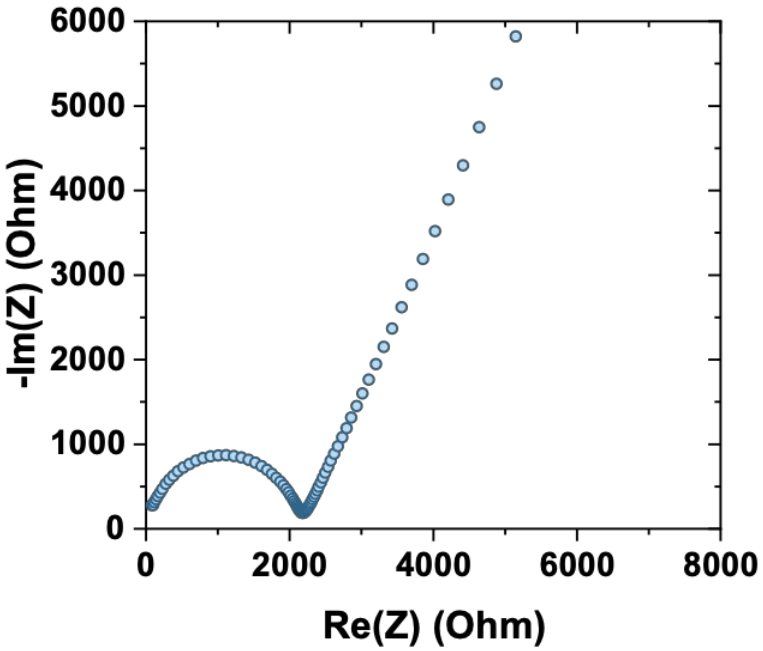

Figure S25. Nyquist plot of LITO measured via electrochemical impedance spectroscopy (EIS) at room temperature. The Li conductivity based on fitting is 0.14 mS/cm.

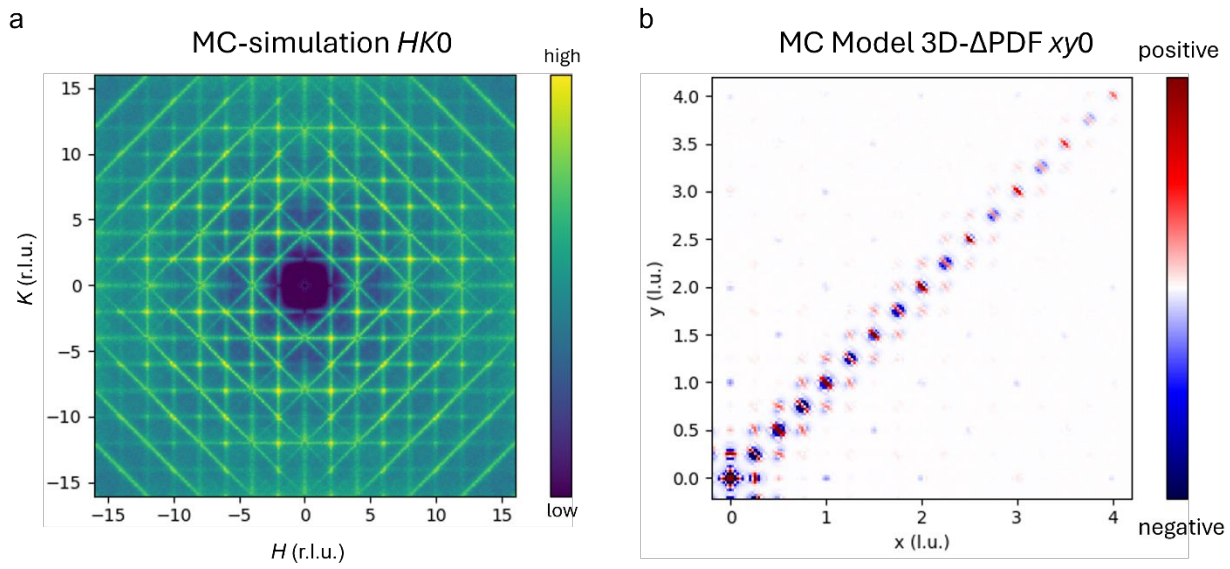

Figure S26. MC model with 100% In occupancy in 16*d* (no Li substitution or chemical SRO) and expanded In-In distances (size-effect only). **a.** Simulated diffuse scattering pattern in *HK*0 showing predominant streaks in <110> directions. **b**. 3D-ΔPDF generated from a Fourier transform of the simulated diffraction pattern, showing only transverse displacements for vectors on the face-diagonal axis.

Supplementary References:

(1) Zeng, Y.; Ouyang, B.; Liu, J.; Byeon, Y.-W.; Cai, Z.; Miara, L. J.; Wang, Y.; Ceder, G., High-entropy mechanism to boost ionic conductivity. *Science* **2022,** *378* (6626), 1320-1324.

(2) Ewald, P. P., Die Berechnung optischer und elektrostatischer Gitterpotentiale. *Annalen der Physik* **1921,** *369* (3), 253-287.

(3) Chen, Y.; Lun, Z.; Zhao, X.; Koirala, K. P.; Li, L.; Sun, Y.; O'Keefe, C. A.; Yang, X.; Cai, Z.; Wang, C.; Ji, H.; Grey, C. P.; Ouyang, B.; Ceder, G., Unlocking Li superionic conductivity in face-centred cubic oxides via face-sharing configurations. *Nat Mater* **2024,** *23* (4), 535-542.